Recent Advances in Welding Processes for High-Entropy Alloys: A Comprehensive Review

Min Li [1,2], Monsak Pimsarn [3], Varesa Chuwattanakul [3,*], and Smith Eiamsa-ard [1]

[1] School of Industrial and Engineering Technology, Mahanakorn University of Technology, Bangkok, Thailand
[2] Sino-German College of Intelligent Manufacturing, Shenzhen City Polytechnic, Shenzhen, China
[3] School of Engineering, King Mongkut's Institute of Technology Ladkrabang, Bangkok, Thailand
Email: 6719880002@mut.ac.th (M.L.); monsak.pi@kmitl.ac.th (M.P.); varesa.ch@kmitl.ac.th (V.C.); smith@mut.ac.th (S.E.)
*Corresponding author

***Abstract*—High-Entropy Alloys (HEAs) have gained attention for their exceptional mechanical properties, corrosion resistance, and unique microstructure. However, welding HEAs remains challenging, attributed to intricate microstructures, inadequate thermal conductivity, and elevated melting points. This review systematically summarizes recent advances in metal welding of HEAs with both similar and dissimilar alloys, including stainless steel, titanium alloys, aluminum alloys, and nickel-based alloys. Welding techniques, including Gas Metal Arc Welding (GMAW), Laser Welding (LW), Electron Beam Welding (EBW), and Gas Tungsten Arc Welding (GTAW) are critically compared in terms of joint microstructure, mechanical performance, and corrosion behavior. The influence of filler composition, heat treatment, and process parameters on weld quality are discussed. Key challenges, including microstructure evolution under complex service conditions and controlling brittle intermetallic phases, are identified. Finally, potential research directions and application prospects of HEA welding in advanced manufacturing are outlined.**

***Keywords*—high-entropy alloys, welding processes, microstructure, mechanical properties**

I. Introduction

As industrial requirements evolve, the need for materials exhibiting enhanced performance under extreme conditions has risen. High-Entropy Alloys (HEAs) have become a highly promising candidate material for such application scenarios due to their excellent mechanical strength, corrosion resistance, and thermal stability [1–3]. In recent years, investigation of these alloys has focused on the design, microstructure, and performance analysis of cast and heat-treated alloy systems for predicting engineering applications. When large blocks of the alloys are formulated by casting or solidification methods, component segregation makes them difficult to melt. Therefore, it is particularly important to join high-entropy alloys by welding. However, their weldability remains a significant challenge, owing to their low thermal conductivity, elevated melting points, and complex microstructure [4–6].

In the welding of similar metallic materials, there has been considerable debate regarding the most efficient and practical welding techniques [7, 8]. This is particularly important as modern industrial applications require materials that can perform reliably under harsh conditions. HEA welding techniques have the potential to offer superior performance in several industrial sectors, including energy, transportation, and aerospace [9–12]. In aerospace, HEAs offer excellent strength and high-temperature stability. These properties make them ideal for components like turbine blades and structural parts that face extreme stress and temperature fluctuations. In the energy sector, HEAs are being explored for applications in gas turbines, nuclear reactors, and power plants. Their resistance to corrosion and oxidation under high temperatures helps improve the longevity and efficiency of these systems. However, the differing physical and chemical properties of the materials involved, including their thermal expansion coefficients, and solubility, lead to significant challenges during welding [13, 14]. The formation of brittle phases at the interface due to Intermetallic Compound (IMC) formation remains a major obstacle in welding dissimilar metals, including HEAs. The presence of IMCs, which have low ductility and limited slip systems, can severely degrade the strength and durability of welded joints [15, 16]. Several solutions have been proposed to address these challenges.

First, changes in welding parameters, such as heat input, temperature, and duration, help optimize the welding interface [17, 18]. Second, changing the formulation of the welding filler component can regulate and optimize the local chemical composition at the interface between high-melting-point solder and brazing materials [19–21]. Third, using intermediate layer materials can isolate two materials being welded to prevent elemental diffusion [22–24].

Currently, the metal welding technology of high-entropy alloys has achieved important research

Manuscript received October 9, 2025; revised November 20, 2025; accepted January 13, 2026; published April 23, 2026.

results. An array of welding methods for HEAs and dissimilar alloys, such as Brazing Welding (BW) [25, 26], Diffusion Welding (DFW) [27, 28], Gas Tungsten Arc Welding (GTAW) [29, 30], Laser Welding (LW) [31, 32], Friction Stir Welding (FSW) and Electron Beam Welding (EBW) have been evaluated [33–35]. For example, Lu *et al.* [36] at Dalian University of Technology first proposed the concept of eutectic high-entropy alloy design. They found that it is composed of Face-Centered Cubic (FCC) and B2 layers with different degrees of hardness. Studies indicate that $AlCoCrFeNi_{2.1}$ shows superior strength and improved elongation properties. It has great tensile strength. Vikram *et al.* [37] explored the microstructure of $AlCoCrFeNi_{2.1}$ at high temperatures. This material is manufactured using a laser engineering net forming process. Microstructural studies revealed phases composed of dendritic and eutectic features. Following solidification, the L12 phase preferentially precipitates and shows a dendritic form in the local structure. While the eutectic structure is made up of a layered arrangement of L12 and BCC phases, rapid cooling causes the L12 phase to predominate in the dendritic area. The L12 phase has an FCC structure. The nearly equiatomic distribution of Co, Cr, and Fe maintains the stability of the L12 phase by increasing the relative configurationally entropy and, consequently, stability at high temperatures. According to thermal analysis, L12 may undergo a phase transition at temperatures above 900 °C. In some areas, the grid's cooling capacity is reduced. This high-entropy alloy exhibits enhanced strength and ductility.

Welding performance will be impacted by changes in the metallographic structure and grain formation in high-entropy alloy welds. This study analyzes the key factors that influence the welding of high-entropy alloys. It also summarizes the welding methods used for HEAs and dissimilar metals such as stainless steel, titanium, aluminum, and nickel, as shown in Table A in Appendix. The challenges imposed by each method, proposed solutions, and advancements in welding technology must be considered. Various welding techniques provide unique benefits when utilized for HEAs. GTAW gives superior control and is appropriate for thin materials, whereas laser welding delivers great precision, minimal distortion, and is optimal for aerospace applications. Electron beam welding is effective for thick plates necessitating deep penetration. Solid-state methods like friction stir welding and diffusion bonding minimize flaws and yield refined microstructures, rendering them appropriate for high-performance or dissimilar HEA joints. Table I presents a review of the advantages, limits, and appropriate circumstances for each technique.

TABLE I. SUMMARY OF WELDING METHODS FOR HAZS

Welding Method	Advantages	Limitations	Best Conditions/Applications
GTAW	Stable arc and high weld quality; good control of heat input; suitable for thin sections	Lower efficiency; larger Heat-Affected Zone (HAZ); potential grain coarsening	Precision welding; thin HEA sheets; applications requiring good heat control
Laser Welding	Very narrow HAZ; high welding speed; low distortion; suitable for dissimilar HEA joints	Higher equipment cost; sensitive to joint fit-up; possible porosity	High-precision industrial welding; aerospace components; low-distortion HEA joints
Electron Beam Welding	Deep penetration; low contamination; fine microstructure	Requires vacuum environment; complex equipment	Thick HEA plates; aerospace and nuclear applications requiring deep, clean welds
Diffusion Bonding	No melting; avoids solidification defects; suitable for ceramics and dissimilar metals	Long processing time; requires high temperature and pressure	High-precision components; aerospace and microelectronics
Brazing	Low joining temperature; good for brittle HEAs; suitable for complex shapes	Lower joint strength; filler compatibility needed	Repair work; joining HEAs where low thermal impact is required

II. HIGH-ENTROPY ALLOYS AND STAINLESS STEEL

A. Optimization of Welding Methods and Process Parameters

Stainless steel serves as a widely utilized structural material in the field of welding. It has outstanding qualities including minimal oxidation, high durability, and favorable mechanical characteristics [38]. HEAs and stainless steel, especially the 304 and 316 series, have similar density and thermal expansion, aiding to produce good metallurgical bonding. Sokkalingam *et al.* [39] welded $Al_{0.1}CoCrFeNi$ and 304 stainless steel using tungsten arc welding. After welding, the microstructure transformed from columnar dendritic to equiaxed dendritic crystals. There was a significant grain coarsening. The joint exhibits a tensile strength of 590 MPa, making it suitable for use as a structural material.

Commonly used welding methods include GTAW, laser, diffusion, and rotary friction welding, among others. Laser welding uses a beam of high energy. It provides benefits such as accelerated welding speed, limited welding deformation, and a broad spectrum of compatible materials. Adomako *et al.* [40] explored the laser lap welding of a CoCrFeMnNi and duplex stainless steel heterogeneous metal. They further investigated the impact of thermal treatment of CoCrFeMnNi and duplex stainless steel heterogeneous metal. Research has shown that the integrity of the welded connection is 584 MPa, but its plasticity is low. The plasticity of the joint increases by more than 20% through post-weld heat treatment, while the strength only slightly decreased. Liu *et al.* [41] investigated vacuum diffusion welding of CoCrFeMnNi to stainless steel. CoCrFeMnNi can be

welded to copper, aluminum, and 304 stainless steel due to its excellent machinability and low diffusion properties. The bonding temperature range for CoCrFeMnNi and aluminum is 540–600 °C. CoCrFeMnNi and copper can be effectively bonded at 750–850 °C. CoCrFeMnNi and 304 stainless steels can establish a stable bond at 900–1000 °C.

Process optimization measures for HEAs and stainless-steel welding include appropriately reducing the line energy (<20 J/mm) to reduce hot cracks and δ-ferrite formation. High-purity Ar or an Ar+He mixture is suitable for shielding gas. The flow rate is 10–15 L/min, and the laser spot diameter should be 0.2–0.6 mm for a narrow heat-affected zone and uniform weld. Li *et al.* [42] examined the application of diffusion welding for joining $AlCoCrFeNi_{2.1}$ and 304 stainless steel at temperatures ranging from 900–1000 °C. The welding diffusion zone comprises an intermetallic compound zone containing Fe_2Al_5 and a solid solution zone. Fig. 1 demonstrate the formation of interconnecting structures. The interface on the Eutectic High Entropy Alloy (EHEA) side has FCC and γ-Fe phases due to the uneven diffusion rates of elements among different materials. As the temperature for diffusion welding rises, the shear strength exhibits a slow initial increase followed by a subsequent decline. Fracture occurred on the side of the alloy, far from the interface.

Fig. 1 depicts the changes in the microstructure at the contact interface as the temperature rises from 880 to 1030 °C. 304 stainless steel is on the left side, with $AlCoCrFeNi_{2.1}$ on the right. The material comprises B2 and FCC phases. With increasing temperature, the needle-like precipitates in the FCC phase grow. They consist mostly of a B2 phase with a high concentration of Al and Ni. The B2 phase, with around 45 atomic percent (at. %) Ni, indicates that Ni atoms selectively occupy particular lattice locations inside the B2 unit cell.

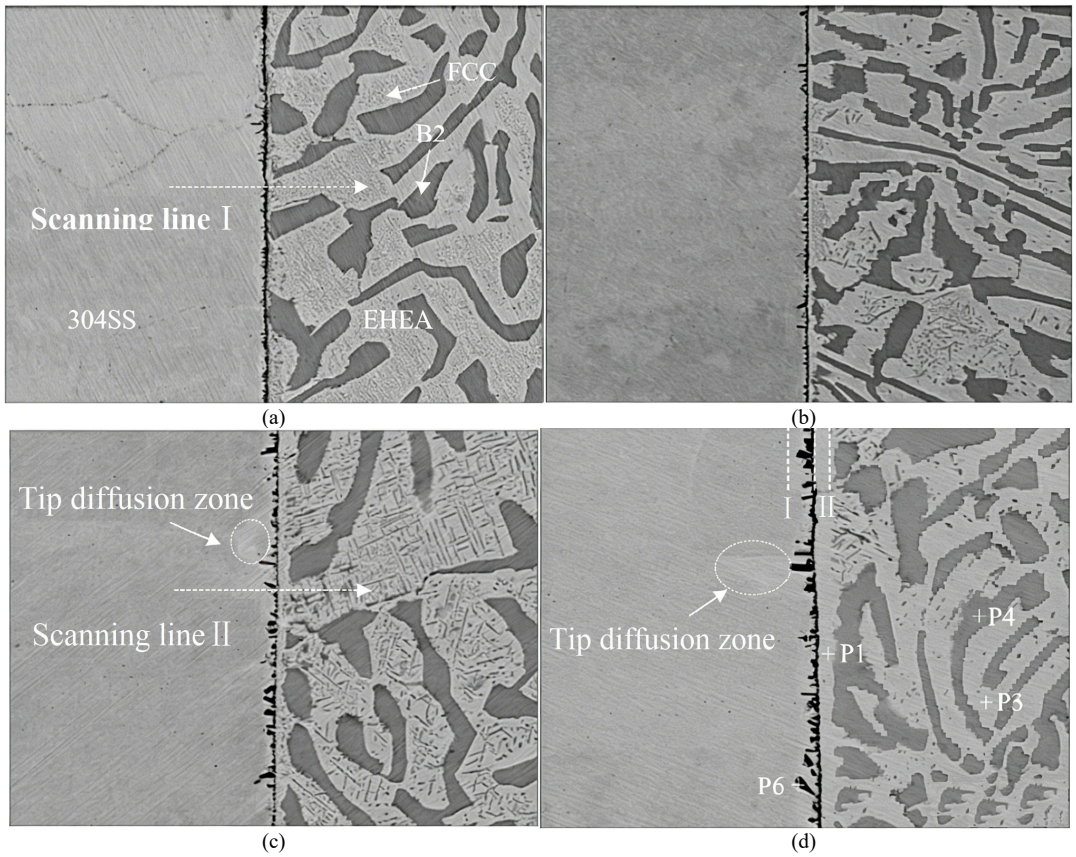

Fig. 1. Microstructures located around the bonding interface of joints at different temperatures: (a) 880 °C; (b) 930 °C; (c) 980 °C; (d) 1030 °C [42].

Within the zones, there is a clear pattern of alternating areas that have lower and higher concentrations of aluminum, but lower concentrations of iron, cobalt, and chromium. The FCC phase achieves stability by distributing Co, Cr, and Fe in almost equal amounts, compensating for the depletion of Ni and Al. This is the principal factor behind the transformation process of the FCC phase, which results in a coarsening and development of the local microstructure. Furthermore, with increased temperature, the lamellar BCC breaks and becomes more refined, ultimately assuming a spherical shape.

The microstructure remains unchanged at 930 °C. Nevertheless, when the bonding temperature increases, the thermal stability of the microstructure progressively declines, leading to increased ductility in the EHEA base metal. According to published reports, the process of diffusion bonding at elevated temperatures leads to the creation of joints by means of viscoplastic deformation, generated by the flow of plastic material. As a result,

although the EHEA base metal becomes weaker at 980 and 1030 °C, the joint becomes stronger.

Zhang *et al.* [43] analyzed BNi-2 to braze CoCrFeNi and AISI 304 steel, resulting in CoCrFeNi/AISI 304 joints. The results indicate that the brazed joint has a diffusion-affected zone. The study found that increasing the brazing temperature improves diffusion and bonding quality. At 1120 °C, the joint exhibits the highest shear strength, 237 MPa, due to reduced CrB precipitation and enhanced bonding. However, excessive temperature (1150 °C) leads to the growth of brittle CrB phases, reducing strength. The study concludes that controlling brazing parameters is crucial for optimizing joint performance.

During vacuum welding of CoCrFeNi/AISI 304 steel, the gap between CoCrFeNi and AISI 304 steel is filled with BNi-2 through capillary action. Atoms from the base metals (Co, Fe, Cr) dissolve into the molten filler metal, while elements from the filler metal (B, Si) diffuse into the base metals in Fig. 2(a). Boron and silicon diffuse rapidly, particularly along grain boundaries. This diffusion results in the creation of boride precipitates (CrB) within the Diffusion-Affected Zone (DAZ). Continued diffusion increases the local melting point in the Isothermal Solidification Zone (ISZ), as shown in Fig. 2(b).

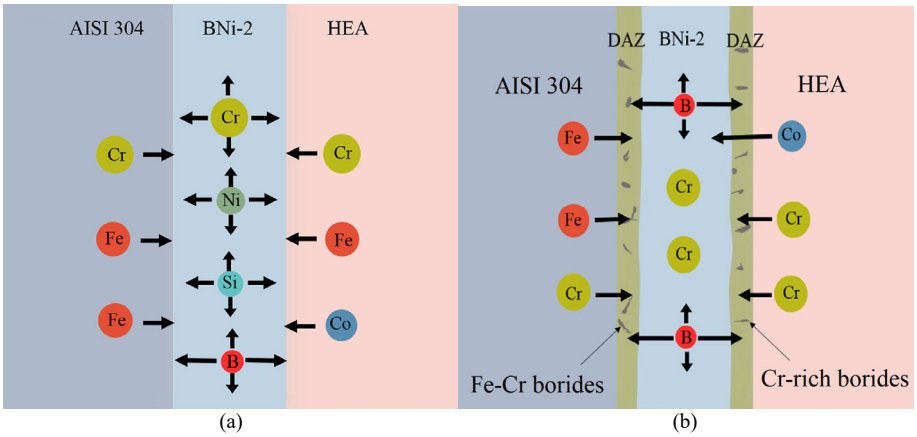

Fig. 2. Microstructural evolution model. (a) atomic cross interface diffusion; (b) the formation of boride phases [43].

Li *et al.* [44] employed solid phase diffusion welding to join CoCrFeNiCu and stainless steel at different temperatures. Solid phase diffusion can achieve connection of the two alloys, but holes remain at the interface at low temperatures. With increased temperature, dispersion is enhanced and the surface openings disappear, while the material becomes denser. No intermetallic compounds are found in the diffusion layer, and a full solid solution structure is formed.

Wang *et al.* [45] developed an Ag72Cu brazing filler metal to achieve brazing of CrMnFeCoNi and 304 stainless steels. They observed significant penetration between the base metal/brazing seam interfaces. In the development of different joint microstructures, the impetus is reduced as annealing temperatures increase. This results in a continuously reduced grain boundary density, which restricts penetration pathways, and the progressively stable grain boundaries in HEAs. During the brazing process, direct mutual diffusion is relatively limited. The atoms originate from the dissolution of the HEAs during brazing. Adjusting intergranular penetration reduces stress concentration on the HEA side, preserving the HEA solid solution strengthening effect of manganese.

B. Evolution of Interfacial Compounds and Characterization of Element Diffusion Behavior

The metallurgical bonding layer between HEAs and stainless steel is formed mainly through elemental interdiffusion. The Fe, Ni, and Cr elements in the two can form a continuous solid solution, thereby improving the bonding strength. However, some reactions may still occur throughout the welding process.

(1) At high temperatures, Al, Ti, and other elements react with Fe and Cr in stainless steel to form Al-rich or Ti-rich intermetallic compounds.

(2) The high Cr content region may induce the HEAs precipitation of σ- or χ-phases, reducing the plasticity. Soleimani *et al.* [46] used contrasting laser welding techniques for Inconel 600 (a nickel-based super alloy) and Duplex 2205 stainless steel. Augmenting laser power elevates the fusion zone temperature and increases the melt pool depth. Variations in focal distance modify heat dispersion, affecting solidification and grain structure in various areas. BM, FZ, and Heat-Affected Zone (HAZ) demonstrate unique grain structure alterations resulting from heat gradients during welding. Inconel 600 features an austenitic FCC matrix characterized by equiaxed 20 μm grains, along with annealing twins. Duplex 2205 possesses an austenitic-ferritic microstructure characterized by coarse ferrite grains and finer austenite grains. Fig. 3 shows that the FZ predominantly displays a cellular and columnar dendritic morphology, with grains oriented along the heat gradient. At elevated laser power (>400 W), more refined dendrites develop owing to enhanced cooling rates.

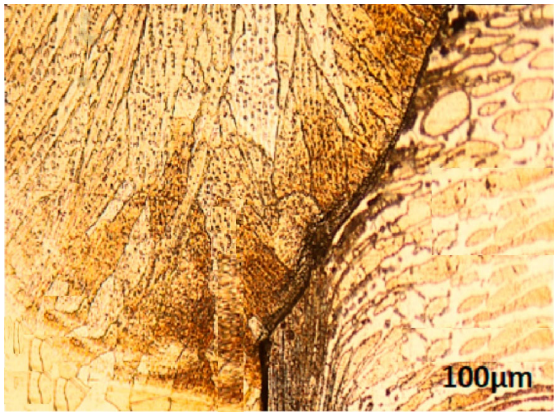

Fig. 3. The microstructure of a welded segment [46].

EDS examination indicates the existence of Mo-rich phases within the interdendritic areas, which diminishes ductility. The fusion zone has a nickel concentration of around 43% adjacent to Inconel 600, whereas the iron level increases to about 26% in Duplex 2205. A thin unmixed zone is present near Duplex 2205, attributed to its elevated melting temperature (about 50 °C higher than Inconel 600), which inhibits complete metallurgical bonding. Grain coarsening occurs due to thermal input, leading to grain expansion of around 200–300 µm. The FCC phase is maintained, but there is increased twinning and dislocation density. Ferrite is converted to austenite, modifying the ferrite-austenite ratio. Grain refinement of approximately 10–25 µm transpires due to fast cooling.

The formation of δ-ferrite is closely related to heat input and cooling rate. Greater heat input is conducive to δ-phase formation. Effective methods to control interfacial reactions include reducing heat input, adopting multi-layer and multi-pass welding technology, and introducing transition layers to buffer the elemental diffusion gradient. Zarei *et al.* [47] investigated the welding of two distinct types of stainless steel using a fiber laser to join martensitic AISI 1060 carbon steel. The welded joints are influenced by thermal input, cooling rate, and alloy composition. Increasing laser power results in an expansion of the depth and breadth of the melt pool. This disparity arises from the different thermal conductivities of the two materials. Increased welding rates result in diminished heat input per unit area, which consequently reduces the size of the melt pool. The mechanical performance of the joints is contingent upon the microstructural attributes. The fusion zone in the AISI 1060/AISI 420 joint displays elevated hardness resulting from martensitic alteration on the AISI 1060 side. The coexistence of austenitic and ferritic phases in the AISI 420 area enhances toughness. Excessive heat input, however, results in grain coarsening, hence diminishing overall joint strength. The fusion zone of the AISI 1060/AISI 304 joint comprises a combination of martensite and preserved austenite, facilitating a balance between strength and ductility. A transformation in the heat-affected zone of AISI 304 leads to grain refinement, hence improving toughness. Fig. 4(a) and (b) illustrates pronounced coarsening of grains in the FAZ of ferritic steel. The narrow HAZ includes rough-grained ferrite, formed due to rapid cooling and reduced heat input during the welding process. Coarse ferrite grains and grain boundaries in the HAZ are formed due to the partial transition of ferrite particles into austenite at high temperatures, which subsequently remain in the structure during cooling. Furthermore, Fig. 4(c) and (d) clearly demonstrates a reduction in both the quantity and size of carbides next to the heat-affected zone, attributable to the significant temperature gradient established between the FZ and the BM. Moreover, welding imperfections, including cracks, are evident near the AISI 1060 base metal.

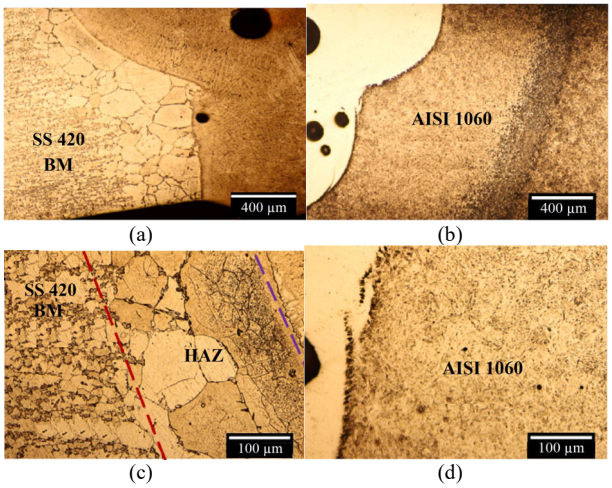

Fig. 4. Microstructural variations of the welded junction using a 400 W laser and a 250 mm/min welding speed: (a) AISI 420 BM and FZ; (b) AISI 1060 BM and FZ; (c) HAZ of AISI 420; (d) HAZ of AISI 1060 [47].

Tao *et al.* [48] welded 7.5 mm 304 austenitic steel utilizing a high-powered fiber laser. Modulating these parameters can reduce defects, achieving penetration and stability for well-formed welds. Fast welding generated a nail-shaped weld, while slow welding produced a peanut-shaped weld. The weld microstructure was mostly austenite with little ferrite, indicating that solidification followed the pseudo-binary phase diagram's F-A mode. The solidification process of the weld zone progressed via a series of transformations: liquid (L) → delta ferrite (δ) → delta ferrite + austenite (γ) → completely austenite (γ). The microstructure fluctuated according to the weld configuration and energy input.

Fig. 5 illustrate that the nail-shaped welds are comprised of austenite and ferrite. The ferrite distribution varied by region: 1.4% at the top, 2.4% in the middle, and 1.3% at the bottom. Conversely, peanut-shaped welds exhibited a reduced ferrite content (0.5%). This resulted from extended high temperatures and gradual cooling, facilitating a complete δ → γ transformation. The upper weld, subjected to elevated temperatures and prolonged cooling, had the largest grain structure. The central and lower weld sections, which cooled more rapidly, had finer granules.

In summary, research progress has been made in the dissimilar welding of stainless steel and high-entropy alloys in terms of process selection, interfacial reaction

mechanisms, microstructure evolution, and mechanical properties. Fusion welding is suitable for complex structures, but requires suppressing the formation of ferrite and brittle phases. Laser welding effectively refines weld microstructure, balancing strength and ductility. Solid-phase welding offers advantages in terms of interface uniformity and toughness retention.

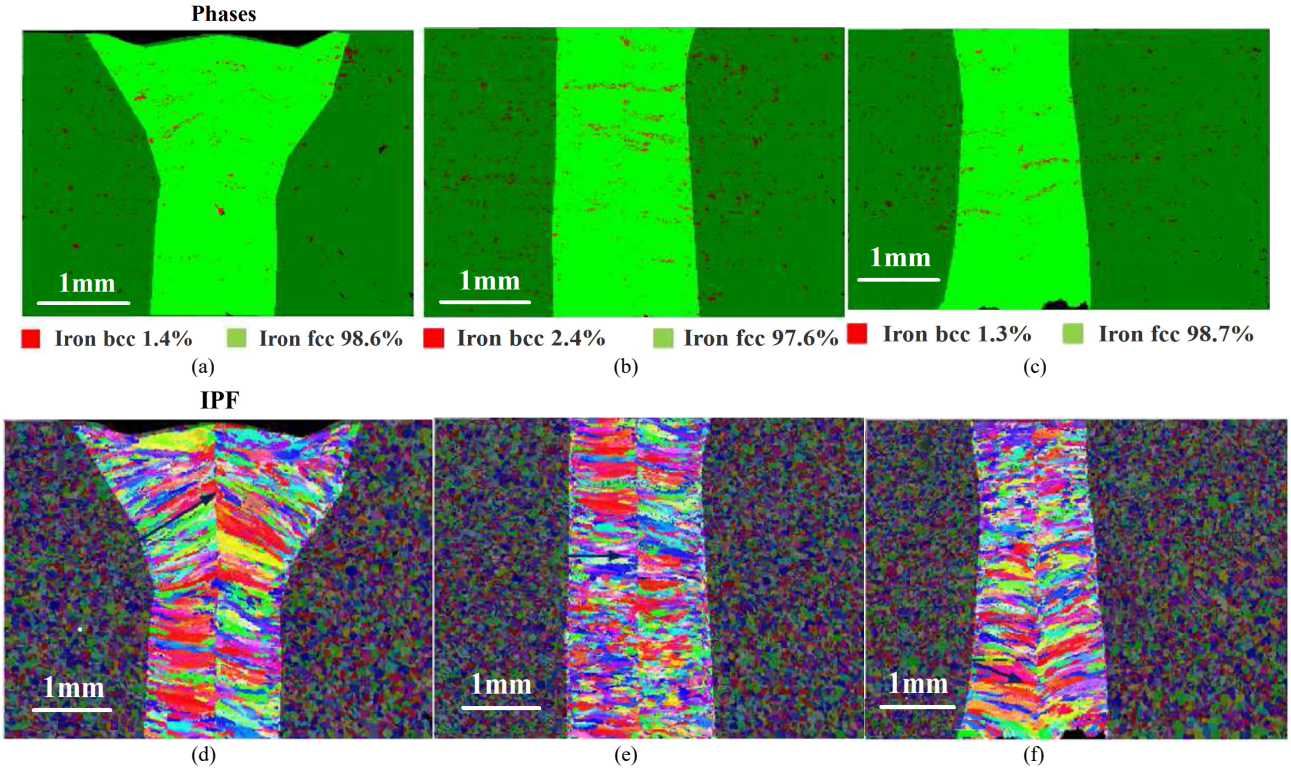

Fig. 5. EBSD analysis of the nail-shaped welded junction at several sites, including phase and Inverse Pole Figure (IPF): (a) Phase top weld; (b) Phase mid-weld; (c) Phase lower weld; (d) IPF top weld; (e) IPF mid-weld; (f) IPF lower weld [48].

III. Dissimilar Welding of High-Entropy and Ti Alloys

A. Improvement of Welding Methods and Control of Process Parameters

The combination of HEAs and titanium alloys can achieve a balance between lightweight, high strength, and corrosion resistance. However, owing to the mismatched thermo-physical properties (HEAs typically have high melting points and low diffusion rates, while titanium alloys have poor thermal conductivity and high activity), brittle intermetallic compounds are easily formed during welding, thereby limiting joint performance.

Research on high-entropy alloy/titanium alloy dissimilar metal welding mostly focuses on diffusion welding. Du *et al.* [49] used diffusion welding to achieve diffusion bonding of $Al_5(TiZrHfNb)_{95}$ and Ti_2AlNb. A brittle Al_3Zr_5 phase appeared as discrete particles along the bonding interface. These Al_3Zr_5 particles gradually elongated and dissolved. The emergence of the Al_3Zr_5 phase was ascribed to its lower Gibbs free energy compared to other potential intermetallic compounds within the examined temperature range. Mechanical testing revealed that the highest shear strength of the joint was achieved at a bonding temperature of 1100 °C. This improvement in strength was associated with the reduction and eventual dissolution of the brittle Al_3Zr_5 phase at higher temperatures, leading to a more homogeneous and robust bonding interface.

B. Interface Microstructure and Brittle Phase Formation Mechanism

1) Elemental diffusion behavior

The metallurgical bonding between HEAs and titanium alloys is mainly achieved through elemental diffusion and new phase formation during interface bonding. Elements like Ni, Fe, and Co readily permeate the Ti matrix, while Ti also migrates toward the HEAs side. This bidirectional diffusion forms a complex transition layer. Peng *et al.* [50] investigated the process of diffusion bonding between the TC4 titanium alloy and Al_5 $(HfNbTiZr)_{95}$. Both sets of alloys were effectively joined under a pressure of 5 MPa and at temperatures ranging from 800–1000 °C for 60 min. The joint's diffusion connecting seam was divided into regions. Region I is the reaction zone containing needle-shaped titanium, while Region II is a reaction zone that maintains the alignment shown in Fig. 6. Furthermore, the investigation elucidated the results of connection temperature. As the temperature of the connection increases, all areas where reactions occur expand in a curved shape. The strength of the joint's resistance to shearing ranges from 55.56–777.1 MPa. Using a 950 °C connection temperature for 60 min, the joint achieves an

ultimate shear strength. A fracture surface is observed on the TC4 matrix, indicating a typical ductile fracture mechanism.

Fig. 6 illustrates the standard microstructure at the joint contact. The junction was formed by bonding under a 5 MPa pressure. Fig. 6(a) shows a close-up view of Zone I, consisting of distinct A and B phases. Based on EDS data, they consist of Ti and Al with a small amount of V, according to research on the TC4 alloy. Furthermore, the microstructure does not exhibit a clear demarcation. However, there is a substantial decrease in the titanium concentration from the former to the latter, as illustrated in Fig. 6(b). Zone II constitutes an uninterrupted solid mixture, implying that the structure closely resembles the Refractory High Entropy Alloy (RHEA).

2) Metallurgical bonding characteristics

The interface transition zone in laser welding is narrow and the compound formation is limited. The diffusion welding interface is relatively flat and the structure is uniform, but an excessive holding time will aggravate the deposition of brittle phases. In the diffusion welding of $Al_{0.85}CoCrFeNi$ and TiAl alloys [51], the highest achievable shear strength was approximately 70 MPa. By subjecting the material to 850 °C for 1.5 h at a 30 MPa pressure, the failure path moved from the γ-TiAl layer, which was fortified by a solid solution and contained FeNi and AlNiTi compounds, into a Cr(Fe, Co) solid solution, according to fracture analysis.

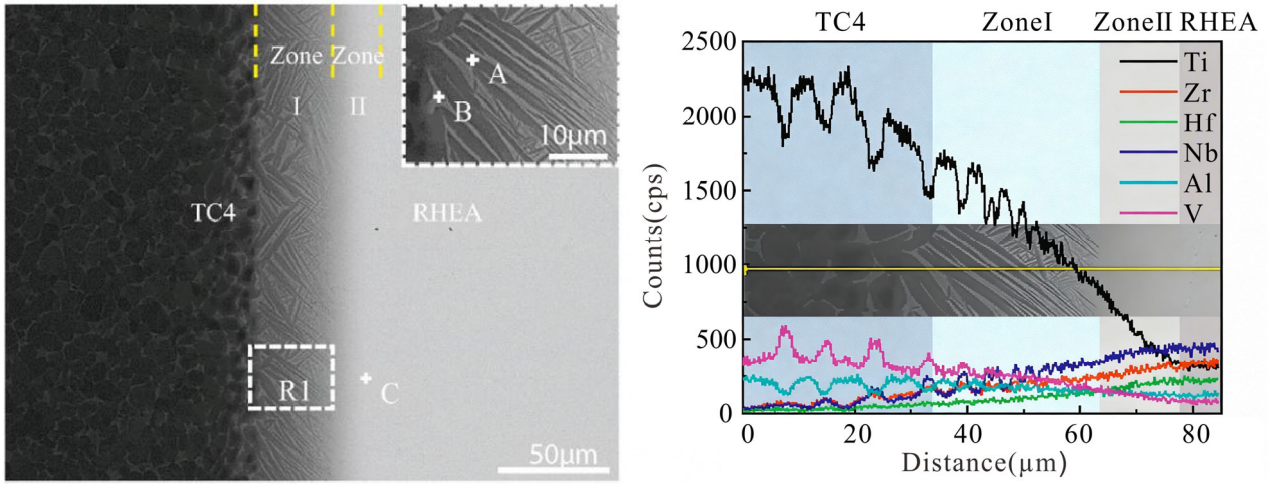

(a) (b)

Fig. 6. Typical interface characterization of a joint. (a) morphology; (b) elemental distribution across the joint [50].

3) Formation of brittle compounds

At high temperature, Ti, Al and Ni easily form intermetallic compounds like TiAl and TiNi, which reduce joint ductility. Li *et al.* [52] achieved a metallurgical interlocking structure in a diffusion welded joint of $AlCoCrFeNi_{2.1}$/TiAl alloy, as shown in Fig. 7. The bonding process created several response zones at the interface, with differences in phase composition based on the foundation material. The diffusing zone adjacent to the FCC phase has two layers of reaction, including a rod-like B2 phase and mixed TiAl-based phases. Conversely, the diffusion zone adjacent to the B2 phase comprises three layers. The development of these layers exhibits a parabolic tendency, influenced by the dispersion of Al and Ni. The penetration and convex formations produce an interlocking effect, hence augmenting joint strength. A maximum shear strength of 449 MPa was attained at 950 °C. However, additional temperature elevations result in excessive layer proliferation and diminished mechanical performance. The shear strength of this joint is far superior to that of an $Al_{0.85}CoCrFeNi$ single-phase high entropy alloy/TiAl alloy joint with no interlocking structure. Establishment of this metallurgical interlocking structure leads to a novel concept for studying the interface regulation of alloy heterogeneous metal joints.

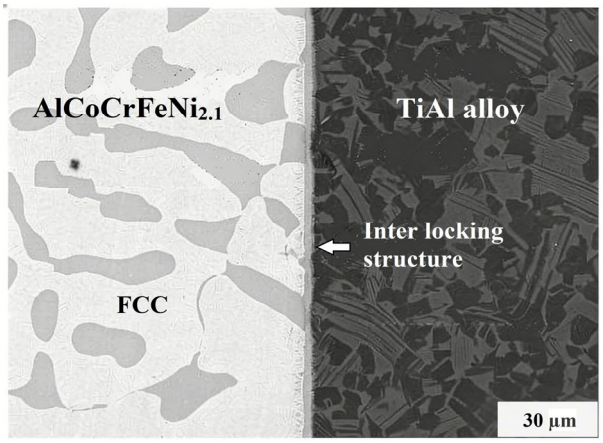

Fig. 7. Interface morphology of $AlCoCrFeNi_{2.1}$/TiAl alloy diffusion welded joint [52].

Overall, dissimilar welding of HEAs and titanium alloys still presents challenges in process compatibility. The main issues are the formation of brittle compounds at the interface and stress concentrations caused by differences in thermo-physical properties. By reducing

heat input, optimizing parameter combinations, and introducing an intermediate transition layer, joint strength can be achieved to 85%–95% of the parent material, while maintaining reasonable plasticity.

IV. Dissimilar Welding of High-Entropy and Al Alloys

A. Process Adaptability and Welding Heat Input Control

Welding high-entropy alloys to aluminum alloys is significantly more challenging than joining them to stainless steel or titanium alloys. Aluminum alloys have relatively low melting points (approximately 600 °C), while most HEAs melt at over 1200 °C. This results in significant differences in the molten pool temperature during welding, which can easily lead to asymmetric solidification and uneven microstructure in the weld.

While fusion welding methods (such as GTAW and laser welding) can achieve interfacial bonding, high heat input often induces thick, brittle IMCs, significantly reducing joint ductility. Studies have shown that when the heat input exceeds 25 J/mm, Al-Fe and Al-Ni compounds rapidly thicken, leading to a sharp drop in joint strength. Therefore, low-heat-input processes are preferred. FSW and explosive welding are solid-state joining methods that significantly suppress the continuous formation of IMCs and form ultrafine grains and a metallurgical bonding layer at the interface. They are currently considered the most promising methods for HEA/aluminum alloy welding. Arab *et al.* [53] examined explosive welding of 6061 aluminum alloy sheets and AlCoCrFeNi. The strength of the aluminum alloy side post-welding remained unaffected by the shock wave produced by the explosion. The aluminum alloy's strength adjacent to the interfacial region is attributable to the strain-induced grain refinement and accompanying plastic deformation within the intermediate layer. Simultaneously, several fissures were noted in the welded specimens subjected to high-speed collisions.

B. Interfacial Compounds and Elemental Diffusion Behavior

Within the welds joining HEAs and Al alloys, the interfacial reaction and elemental diffusion behavior directly determine the mechanical properties of the joints.

(1) Intermetallic Compound Formation: Aluminum has a strong chemical affinity for elements such as Ni, Fe, and Ti in HEA, easily forming brittle intermetallic compounds such as Al-Ni, Al-Fe, and Al-Ti. These compounds exhibit high hardness but extremely poor ductility, leading to premature joint failure.

(2) Element Diffusion Characteristics: During diffusion welding and FSW, Al atoms diffuse rapidly toward the HEAs, while elements such as Ni and Fe diffuse toward the Al, forming a transition layer. When the diffusion layer thickness is controlled within the 1–3 μm range, the joint achieves good strength. If it exceeds 5 μm, the brittle IMC layer becomes continuous, significantly reducing the joint toughness.

(3) The role of a HEAs as an intermediate layer in aluminum alloy welding involves a multi-element solid solution structure in HEAs that effectively hinders the rapid diffusion of a single element.

Jiang *et al.* [54] studied resistance spot welding of Q235 steel/6061 aluminum alloy dissimilar metals using $Fe_{0.2}CoCrMnNiAl_{0.2}$ as the intermediate layer. They employed the super-solid solubility of a HEA to enhance the welding quality of dissimilar metals. There were semi-elliptical nuggets on both the steel and aluminum sides of the joint section. The nuggets exhibit good morphology and are devoid of macro-cracks, pores, or other weld imperfections. The internal structure of the nuggets is formed by an FCC solid solution phase. The average maximum tensile shear force of the joint reached 1913 N, representing a 130% increase compared to the steel/aluminum direct resistance spot welding joint. Fracture occurs at the Al alloy side nugget. The Al alloy nugget is torn off under tensile shear stress and remains on the surface of the alloy, showing a "button-shaped" failure feature.

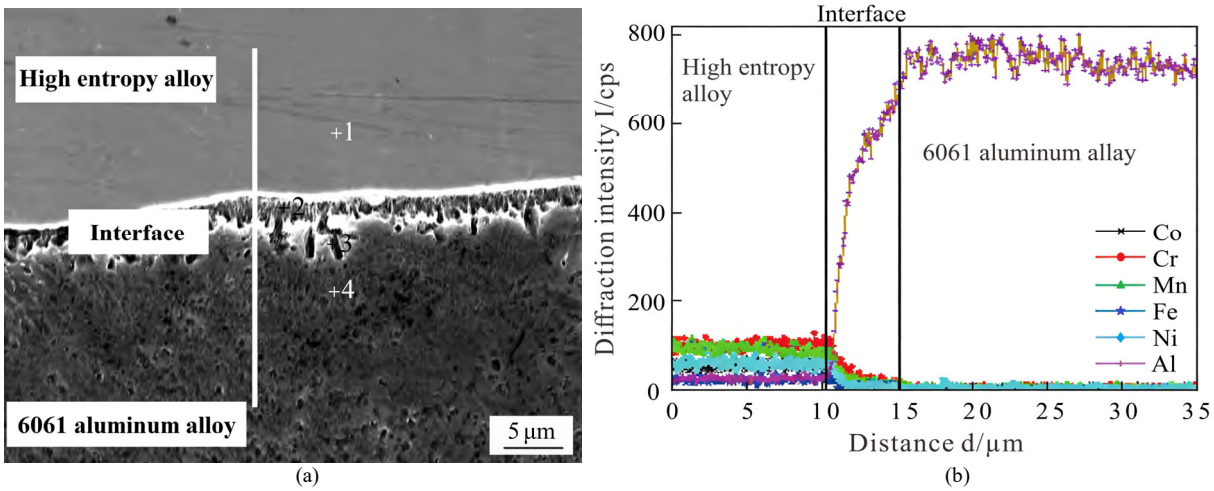

Fig. 8. Microstructure of the interface between HAZs and the 6061-aluminum alloy. (a) SEM image of the interface; (b) EDS line scan [54].

Microstructural analysis of the aluminum alloy side nugget is depicted in Fig. 8(a). A metal interfacial transition layer exists between the high entropy alloy and the 6061-aluminum alloy. EDS line scans show that the aluminum concentration increases continuously from the middle layer to the aluminum alloy nugget, while other concentrations decrease in Fig. 8(b). The Co, Cr, Mn, Ni, and Fe contents are almost zero far away from the interface. Coupling in the metalworking process of the alloy and the aluminum nugget is completed by the wetting and spreading of aluminum liquid across the top of the alloy. An interface transition layer was formed by mutual diffusion of elements.

Azhari-Saray *et al.* [55] examined spot welds of 6061-T6 and St-12 plates, which have different resistances. They compared the weldments with and without an $Al_{0.5}FeCoCrNi$ HEA intermediate layer (0.4, 0.7, 1 μm thick). Without the intermediate layer, no interface on the carbon steel/HEA side was observed. There was a complex IMC on the Al/HEA side. The IMC type changed within the intermediate layer. Its thickness affected the IMC morphology, increasing the tensile shear load. The fracture mechanism was also different.

Fig. 9 presents an SEM micrograph of two different types of 6061AA/carbon steel welding made at different welding currents, electrode forces, and thicknesses. Significant voids are observed that contact during welding, especially when a minimal electrode strain is exerted. Nonetheless, the dimensions of voids diminish as the electrode force is increased. This figure reveals that the use of an HEA interlayer induced the nucleation of voids at the aluminum interface.

When HEAs are used as an intermediate layer, a gradient diffusion layer of an "Al-HEA-matrix" is typically formed at the weld interface. Slow interdiffusion of different elements forms a solidified single-phase region at the interface, alleviating stress concentration and improving interfacial bonding strength.

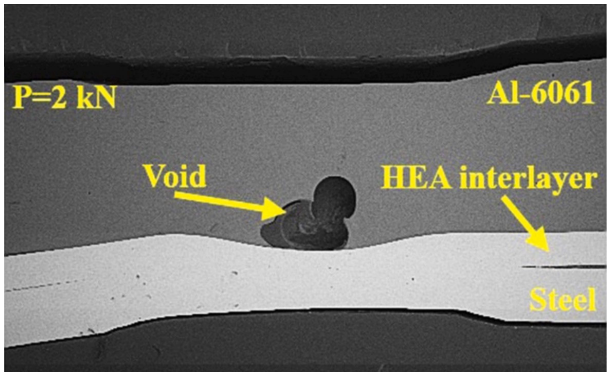

Fig. 9. Low-magnification SEM image of a welded joint [55].

Gu and Zhang [56] examined the laser lap welding of TC4 titanium and 6082 aluminum alloys utilizing a $CoNiCuNb_{0.5}V_{1.5}$ filler to inhibit the production of brittle Ti-Al intermetallic compounds. The HEA filler, utilizing its elevated mixing entropy and slow diffusion effects, promotes solid solution formation while limiting Ti-Al interactions.

Fig. 10 presents SEM imagery that exhibits no apparent macro-defects, and the contact seems to be securely bonded. The reaction interface has a 0.8 μm thick Al_3V compound layer that augments joint strength. The fracture propagates along the HEA/Al interface, exhibiting a combination of ductile and brittle properties. The maximum measured tensile strength is 190 MPa, accompanied by a peak hardness of 600 HV. Effective utilization of an HEA filler significantly inhibits Ti-Al intermetallic compounds, hence enhancing joint quality and mechanical performance.

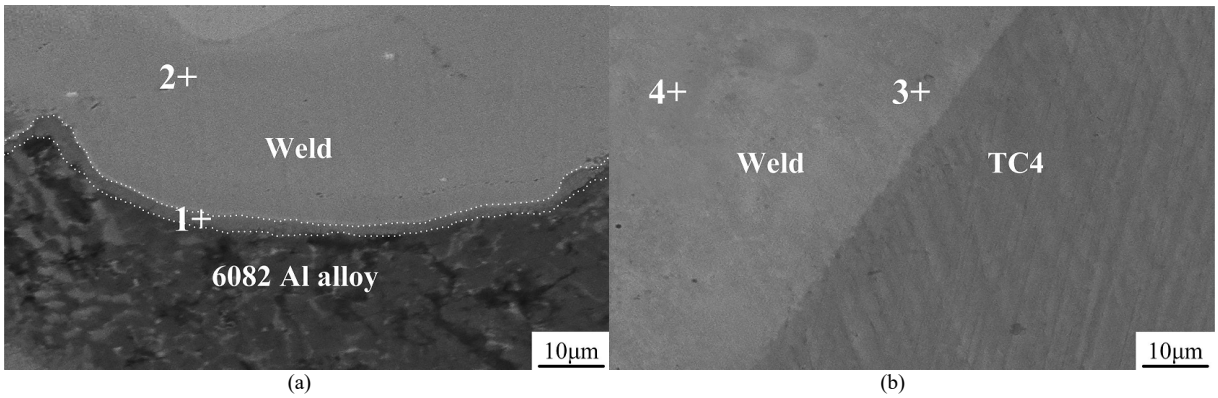

(a) (b)

Fig. 10. SEM image of joint interfaces. (a) HEA/Al reaction interface; (b) Ti/HEA reaction interface [56].

V. Dissimilar Welding of High-Entropy and Nickel Alloys

Nickel-based HAZs constitute a prominent material group. They predominantly consist of nickel, with most nickel-based alloys containing 10%–20% chromium to form a nickel-chromium austenite matrix.

Alloys reinforced by a solid solution are produced by incorporating components such as Cu, Co, and Mo. Strengthening involves solid solutions of nickel-based alloys [57], such as Haynes 230 and Inconel 617, owing to the simplicity of integrating these alloying constituents with carbon compounds. Addition is the principal mechanism by which this alloy produces various carbides. The alloying components are integrated into the austenite matrix, and no brittle phase exists in the alloy to ensure a strengthening effect. Precipitation-strengthened alloys refer to nickel-based

materials [58], such as Nimonic 263 and Inconel 740. After appropriate heat treatment, they form precipitates with Ni in the matrix to strengthen the γ matrix. The precipitation-strengthening phases are usually γ-Ni_3Al and γ-Ni_3Ti, which improve strength by interacting with the matrix and dislocations.

High-entropy alloys are expected to replace high-temperature alloys in the manufacture of key structural parts in aircraft engines. Consequently, it aims to thoroughly characterize the welding of high-entropy and high-temperature alloys. Lei *et al.* [59] analyzed the eutectic-reaction brazing technique for Al0.3CoCrFeNi employing Ni/Nb/Ni interlayers. These interlayers were selected for their capacity to create a eutectic phase with an HEA, facilitating efficient bonding at reduced temperatures. The experimental results indicated that the interlayers effectively facilitate the formation of a eutectic liquid phase, hence improving the wetting and spreading of the filler material. This results in strong joints with enhanced mechanical integrity.

Ni and Cr in nickel-based alloys form a stable solid solution with the same elements in HEAs, thereby reducing the interfacial stress concentration. However, it is notable that excessive segregation of Nb and Mo can induce Laves phase precipitation, while excessive welding heat input facilitates the development of brittle phases, resulting in reduced joint toughness. Li *et al.* [60] examined diffusion joining $AlCoCrFeNi_{2.1}$ and GH4169. With an increased connecting temperature, the Diffusion Zone (DZ) expands, and cavities decrease because of improved elemental diffusion and elevated-temperature creep. Fig. 11 shows a novel FCC phase layer that develops in the DZ, arising from the disparate diffusion rates between the B2 and FCC phases. This layer improves joint shear strength to a maximum of 528 MPa correlated with a bonding temperature of 1050 ℃. Fracture modes transition from brittle to ductile as connecting temperatures increase.

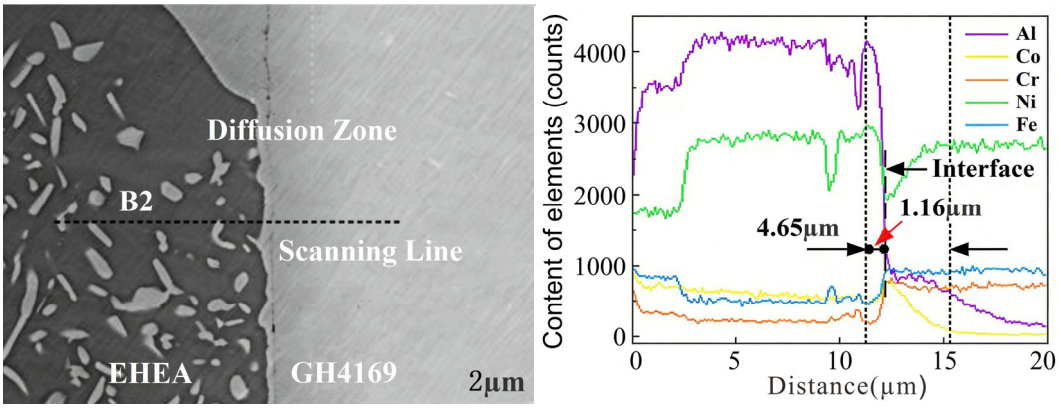

(a) (b)

Fig. 11. Microstructural and compositional analysis across the interface. (a) SEM images of diffusion zone and B2 zone; and (b) EDS line-scan results illustrating the elemental distributions across the interface [60].

VI. Welding Research on High-Entropy Alloys

A. Process Parameter Optimization

The weld interface between two HEAs exhibits better metallurgical compatibility than that between HEAs and conventional alloys [61]. This is primarily due to the multi-principal solid solution structure, similar thermal expansion coefficients, and low diffusion rates common in HEAs. This facilitates the formation of a continuous weld structure and a uniform transition layer, while also preventing the formation of large-scale brittle intermetallic compounds [62].

B. Interfacial Reaction and Metallurgical Bonding Mechanism

The interface typically exhibits a dense metallurgical bond, free of significant porosity and cracks. Fractures often occur in the substrate metal instead of at the boundary, indicating a high bond strength. During friction stir welding and diffusion welding, interfacial recrystallization and refinement are particularly pronounced, forming a uniform equiaxed grain structure, further enhancing interface stability.

Zhu *et al.* [63] performed friction stir welding on $Co_{16}Fe_{28}Ni_{28}Cr_{28}$ and studied the phase structure changes and strength of the resulting welded joints. The phase structure is mainly 70% FCC, with good ductility. The $Co_{16}Fe_{28}Ni_{28}Cr_{28}$ source material exhibited an equiaxed grain structure characteristic of FCC alloys. Application of FSW resulted in substantial grain refinement in the stir zone due to severe plastic deformation and accompanying thermal cycles. The discontinuous recrystallization process, induced by grain boundary bulging, generated new grains that were significantly smaller than those in the original material. The resultant shear texture, defined by the $B/\bar{B}$ {112}<110> orientation, signifies a favored alignment of grains attributable to the directional characteristics of the FSW process.

1) Interfacial phase transition mechanism

In most cases, the interface is dominated by a continuous solid solution of FCC/FCC or FCC+BCC, with relatively few independent brittle phases. However, in HEAs containing Al and Ti, the B2 phase or Ti-Al compounds may still precipitate locally. Their growth must be suppressed by controlling the heat input.

Nam *et al.* [64] examined the impact of post-weld thermal treatment for the weldability of CoCrFeMnN. Following post-weld thermal treatment, the base material's strength was lower than the weld, the FCC phase in the weld did not change, and the number of CrMn oxide inclusions decreased. The twin Weld Metal (WM) produced with a CoCrFeMnNi filler displayed a consistent single-phase FCC structure. The WM containing the CuCrFeMnNi filler exhibited notable phase separation.

The Cu-rich phase showed discrete particles dispersed throughout the WM. Identification of these particles indicated an FCC structure, consistent with the primary matrix, while also showing a higher concentration of Cu. The presence of these Cu-rich particles indicates that incorporation of Cu promotes phase separation during solidification. This leads to a multiple-phase structure comprising the original FCC matrix and a Cu-rich phase, as depicted in Fig. 12.

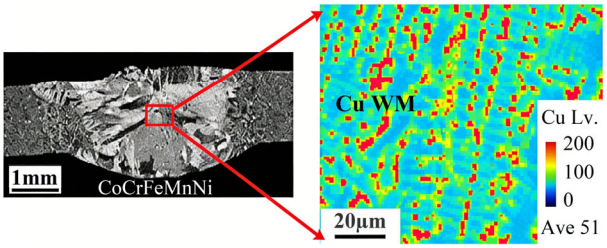

Fig. 12. Influence of a Cu-rich phase on weld properties [64].

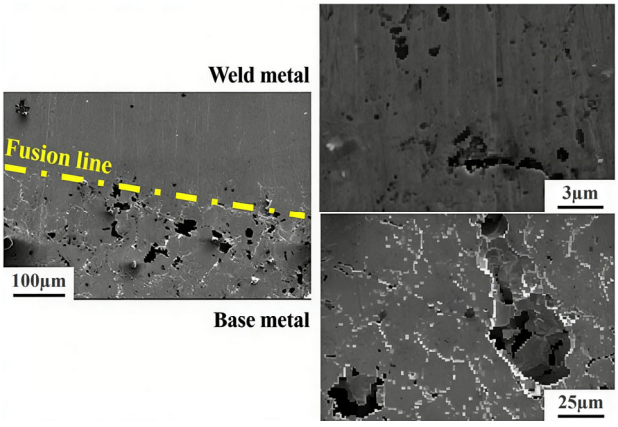

Fig. 13. Metallographic structure diagram of the base metal and fusion zone [65].

Sokkalingam *et al.* [65] utilized laser welding to join HAZs and $Al_{0.5}$CoCrFeNi. The $Al_{0.5}$CoCrFeNi base metal displayed an FCC structure, characterized by equivalent grains about 50 μm in size. Significant microstructural changes were observed in the FZ and HAZs, as depicted in Fig. 13.

In the FZ, rapid solidification produced a finer dendritic structure than observed in the BM. The average grain size in the fusion zone was approximately 20 μm, demonstrating significant grain refinement attributed to the greater cooling rates characteristic of laser welding. The HAZ exhibited partially recrystallized grains with dimensions intermediate between those of the base metal and fusion zone, indicating thermal exposure adequate to modify grain structure without total melting. Improved corrosion resistance in the FZ results from the enhanced grain framework, which facilitates the development of a homogeneous and adherent passive coating. The rapid solidification occurring during laser welding can result in a more uniform elemental distribution, thereby minimizing localized sites of galvanic corrosion.

2) Elemental diffusion behavior

Under laser and electron beam welding conditions, the main elements exhibit relatively uniform interfacial interdiffusion, avoiding severe elemental segregation. Due to the low elemental diffusion rate in HEAs, the interfacial transition layer is typically thin (1–3 μm), which helps maintain strong joints. Kashaev *et al.* [66] investigated the laser welding of CoCrFeNiMn. The alloy base material consisted primarily of coarse columnar grains of the FCC phase, as well as MnS inclusions and fine-scaled Cr-rich $M_{23}C_6$ carbide precipitates. B2 phase precipitation was present in the weld. Precipitation of carbide particles led to a significantly enhanced micro-hardness. Laser welding induces substantial alterations, reducing the grain size in the FZ to between 100 and 300 μm, with elongated grains forming along the solidification front. The welding procedure results in the formation of M_7C_3 carbides. This hardening is associated with carbide precipitation and minor grain refinement, as depicted in Fig. 14.

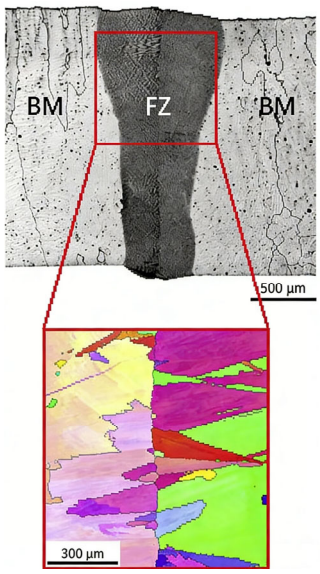

Fig. 14. EBSD analysis of a laser-welded CoCrFeNiMn: the grain morphology across the base metal, fusion zone, and heat-affected zone [66].

Microstructural research during fatigue testing indicates that at lower loads, both situations exhibit heightened dislocation density, predominantly in planar arrays. At elevated stresses, dislocation density further increased, and mechanical twinning became apparent, particularly at values exceeding 350 MPa. Twin structures, around 20–30 nm in thickness, develop in conjunction with dislocation cells. The role of twinning in deformation seems to be less substantial than that of dislocation. Analysis of the fracture surface revealed

characteristic fatigue features, including crack initiation, propagation, and overload fracture. Fatigue cracks generally originate at the surface, traversing crystallographic planes, and advance through the base material, exhibiting fatigue striations and dimples likely caused by MnS inclusions. Carbide particles appear to have little effect on fracture initiation.

Wu *et al.* [67] analyzed the performance of electron beam welding of CrMnFeCoNi. The grain structure within the FZ was governed by the solidifying behavior of the heated pool. Compared with the parent material, deformation twins are more pronounced in the fusion zone. CrMnFeCoNi in its original state has a homogeneous FCC structure with equiaxed grains measuring around 20 μm, attained through blending at 1200 °C, subsequent annealing at 900 °C. The BM displays annealing twins, typical of FCC metals with low stacking fault energy. The initial microstructure is modified during welding due to melting and quick solidification. The FZ has a course, columnar grain structure, extended toward the heat gradient in Fig. 15. In contrast to the BM, which exhibits fine and equiaxed grains, the grains in the FZ develop through epitaxial solidification within the partly melted BM along the fusion boundary.

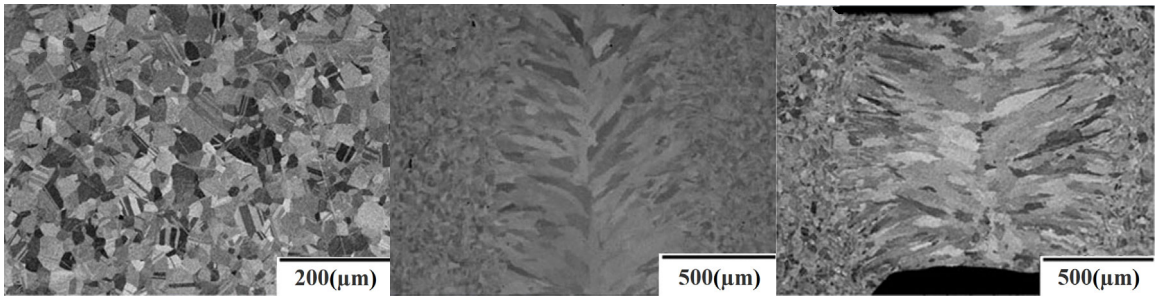

(a) (b) (c)

Fig. 15. Grain change diagram during welding. (a) primary alloys; (b) the superior surface; and (c) the lateral surface of the weld [67].

The HEA/HEA weld interface offers advantages over dissimilar metal welds. These include strong metallurgical compatibility, uniform elemental diffusion, and excellent solid solution continuity. This results in joints with strength and toughness approaching or even equaling those of the parent metal. However, attention should be paid to localized segregation and the formation of brittle phases. Future research should focus on interface regulation, post-weld heat treatment, and service mechanisms under complex loads to ensure long-term stability.

Existing research indicates that welding HEAs to various alloys requires significantly different process parameters and joint microstructure. The characteristics of welded joints and welding methodologies for different HEAs are illustrated in Table B in Appendix.

VII. Conclusions

This study presents a comprehensive comparison of the primary welding methods utilized for high-entropy alloys, covering the gap in previous studies that primarily addressed alloy design, phase evolution, and mechanical properties rather than welding performance. By analyzing the advantages, limitations, and appropriateness of various welding techniques, this study clarifies their functions in practical engineering and facilitates the switch from laboratory research to industrial implementation in aerospace, energy, and advanced manufacturing.

High-entropy alloys have unique properties and show great potential in welding similar and dissimilar materials. To explore their application in engineering structures, numerous studies have focused on the microstructure and process parameters of HAZs welded with the same or different materials. Through the application of new processes such as diffusion welding, brazing, friction Stir welding, and laser welding, researchers have achieved positive results in improving interface metallurgical compatibility, inhibiting the production of brittle compounds and refining the structure. Among them, diffusion welding has been extensively studied for welding HAZs and materials such as steel and aluminum alloys. This can effectively control interfacial reactions and obtain better joints. Rotational friction welding has advantages in self-welding or surface modification of high-entropy alloys, which can refine grain sizes and improve weld performance. GTAW provides effective temperature regulation; nonetheless, it results in an expanded heat-affected zone. Laser and electron beam welding yield narrow heat-affected zones and refined microstructures, rendering them appropriate for high-precision applications. In terms of structural stability, mechanical property retention, and process adaptability, HEAs/nickel-based alloy welding has the greatest advantages, while HEA/aluminum alloy welding is the most difficult.

The findings demonstrate that advanced welding methods may significantly improve joint quality by improving interfacial compatibility, preventing the formation of brittle phases, and refining microstructural characteristics. Nonetheless, the quality of welded connections is highly influenced by the welding technique, especially regarding the management of the heat-affected zone and the preservation of microstructural structure. Although various methods demonstrate

significant potential for welding both the same and different materials, no individual process can comprehensively achieve all welding requirements for HEAs.

Notwithstanding these developments, significant challenges persist. Complex elemental diffusion and interfacial reactions during welding may result in segregation, the formation of brittle intermetallic compounds, and defects such as fractures and pores. The restricted availability of appropriate filler materials, particularly for dissimilar connections, further constrains practical implementation. Furthermore, the long-term performance of HEA welded joints under complex service conditions, such as thermal cycling, fatigue, and corrosion, remains inadequately understood.

Further studies should aim toward improving the weldability of HEAs via optimized alloy design, improved process stability, and the development of standardized welding protocols. Priority areas contain understanding surface reaction mechanisms, developing predictive models for microstructure and mechanical characteristics, and studying innovative or low-temperature welding techniques. Improving performance assessment under extreme operating conditions will be important in progressing the transition of HEA welding from experimental research to practical application in industry.

APPENDIX

TABLE A. HIGH-ENTROPY ALLOY WELDING MATERIALS AND WELDING METHODS

Metal	Brazing	Diffusion Welding	Gas Tungsten Arc Welding	Friction Stir Welding	Explosion Welding	Laser Welding	Electron beam Welding
Stainless steel	√	√	√	√	-	√	-
Ti alloy	√	√	-	-	-	√	-
Aluminum alloy	-	-	-	√	√	√	√
Nickel alloy	√	√	-	√	√	√	-
High-entropy alloys	√	√	√	√	-	√	√

TABLE B. SUMMARY OF WELDING RESEARCH ON HIGH-ENTROPY ALLOYS AND VARIOUS MATERIALS

Investigators	Welding Materials	Welding Method	Process Parameters	Results
Liu *et al.* [41]	CoCrFeMnNi and 304 stainless steel	Vacuum diffusion welding	Holding time: 120 min, temperature: 900–1000 °C, pressure: 28 MPa	The reaction layer is FCC solid solution, pores change with temperature, and the interface gradually changes.
Li *et al.* [42]	$AlCoCrFeNi_{2.1}$ and 304 stainless steel	Vacuum diffusion welding	Holding time: 30–120 min, the best performance at 980 °C	The diffusion zone includes a solid solution zone and a Fe_2Al_5 intermetallic compound zone. As the temperature increase, the zone becomes wider and the B2 phase coarsens to form an interlocking and local solid solution structure.
Zhang *et al.* [43]	CoCrFeNi, AISI 304 stainless steel, BNi - 2 filler metal	Vacuum brazing	Brazing temperature: 1050–1150 °C, brazing time: 30 min, vacuum degree: 10^{-4} Pa. At 1050 °C, there are many voids, and at 1120 °C, the voids disappear.	The brazing seam contains a thermal solidification zone (with CrB precipitates), an isothermal solidification zone (with nickel-based solid solutions), and a diffusion affected zone (containing borides).
Li *et al.* [44]	CoCrFeNiCu and 304 stainless steel	Solid-phase diffusion welding	Holding time: 120 min, temperature: 950–1100 °C, pressure: 20 MPa	A fully solid solution microstructure is formed, without intermetallic compounds, with a granular Cr-rich phase, changing with temperature
Soleimani *et al.* [46]	Inconel 600 and Duplex 2205 stainless steel	Laser welding	Laser power: 250–450 W, welding speed: 200–400 mm/min, focal length: −1.5–+4.5mm, beam deviation: −0.4–+0.4 mm	There are austenite phase and Laves phase in the weld zone, with diverse microstructures, and the grain size in the heat-affected zone changes.
Zarei *et al.* [47]	AISI 1060 carbon steel and 304, 420 stainless steel	Fiber laser welding	Laser power: 250–450 W, welding speed: 150–350 mm/min, focal length: −2–+6 mm, beam deviation: −1–+1 mm	The weld on the 420 steel side has columnar dendrites, etc., and the 304 steel side has dendritic structure; the grain size in the heat-affected zone changes.
Yang *et al.* [38]	2205 duplex stainless steel	Laser welding	Laser power: 1000 W, welding speed: 20–80 mm/s, spot focal length: 0, gas flow rate: 15 L/min	The weld has ferrite and austenite, and the grain morphology changes with welding speed, with precipitates.
Tao *et al.* [48]	304 stainless steel	High-power fiber laser welding	Laser power: 6–10 kW, welding speed: 20–50 mm/s, defocusing amount: −10–+20 mm	The weld has massive austenite and a small amount of ferrite, with nail-shaped and peanut-shaped welds, and different grain sizes.
Peng *et al.* [50]	TC4 titanium alloy, $Al_5(HfNbTiZr)_{95}$	Diffusion welding	Temperature: 800–1000 °C, pressure: 5 MPa, holding time: 60 min	The reaction zone consists of a needle-like titanium structure and a continuous solid solution reaction zone.
Li *et al.* [52]	$AlCoCrFeNi_{2.1}$ and TiAl alloy	Diffusion welding	Temperature: 750–1050 °C, holding time: 30–120 min, pressure: 30 MPa	There are four reaction layers near the FCC phase and three layers near the B2 phase. As the temperature increases, the layer thickness increases, the B2 phase coarsens, and a penetrating and convex structure is formed.

Arab *et al.* [53]	AlCoCrFeNi, Al-6061 aluminum alloy	Explosive welding	A transition layer is formed at the interface with a width of about 1.8μm. Al-6061, transition layer and AlCoCrFeNi are combined at the atomic scale	A transition layer is formed at the interface with a width of about 1.8 μm. Al-6061, the transition layer and AlCoCrFeNi are combined at the atomic level.
Jiang *et al.* [54]	Q235 steel and 5052 aluminum alloy based on high-entropy alloy interlayer	Resistance spot welding	Welding current: 10–13 kA, welding time: 100–300 ms, electrode pressure: 2–4 kN	There are multiple phases, the HEAs interlayer inhibits the formation of intermetallic compounds
Azhari-Saray *et al.* [55]	6061 - T6 aluminum alloy, St - 12 low carbon steel, $Al_{0.5}FeCoCrNi$ interlayer	Resistance spot welding	Electrode force: 2–4.2 kN, welding current: 10–17 kA, welding time: 8 cycles, the thickness of the interlayer is 0.4–1 mm	When there is no interlayer, the Al side of the weld has IMCs such as Fe_2Al_5. It is prone to cracking at the Al/HEA contact, a complicated interlayer mobility coupling (IMC) forms when there is an interlayer, and there is almost no IMC at the carbon steel/HEA interface.
Gu and Zhang [56]	TC4 titanium alloy, 6082 aluminum alloy, $CoNiCuNb_{0.5}V_{1.5}$ filler material	Laser lap welding	Laser power: 660 W, scanning speed: 10 mm/s, laser spot size: 1.5 mm.	The weld zone has a high-entropy alloy zone (FCC and V solid solutions), and the high-entropy alloy/Al interface has an Al_3V compound layer, and a diffusion layer is formed around the contact between Ti and HEA. After optimizing the parameters, welding is achieved, and the formation of Ti - Al IMCs is inhibited
Li *et al.* [60]	$AlCoCrFeNi_{2.1}$ and GH4169 superalloy	Diffusion welding	Temperature: 880–1030 °C, holding time: 30–120 min, pressure: 30 MPa	The FCC phase appears in the diffusion zone, and its width increases with temperature. The B2 phase nanoprecipitates grow first and then dissolve, the δ phase gradually disappears, and the voids decrease.
Zheng *et al.* [61]	$Al_{0.3}CoCrFeNi$, FeCoCrNiCu/Ti composite interlayer	Brazing	Brazing temperature: 1100–1180 °C, holding time: 1–20 min, pressure: 1.5 kPa	Composed of Ti(s, s), Cu(s, s) and FCC phase containing multiple elements, changing with brazing temperature and time.
Zhu *et al.* [63]	$Co_{16}Fe_{28}Ni_{28}Cr_{28}$	Friction stir welding	Rotational speed: 400–800 rpm, welding speed: 50–150 mm/min, downward pressure: 0.1–0.3 mm	The BM exhibits a FCC structure with equiaxed grains. Low-Angle Boundaries (LABs) form, increasing dislocation density near the grain boundaries. Grain subdivision occurs, contributing to discontinuous recrystallization.
Nam *et al.* [64]	CoCrFeMnNi	Gas shielded welding	Welding current:80–120A; Welding voltage: 12–20 V; Speed: 1–3 mm/s; Shielding gas: pure argon or argon-helium mixture, flow rate 10 L/min	Welds with the CuCrFeMnNi filler demonstrated phase separation, resulting in the formation of a Cu-rich phase in conjunction with the basic FCC structure.
Sokkalingam *et al.* [65]	$Al_{0.5}CoCrFeNi$	Laser welding	Laser power: 1500–2000 W, welding speed: 15–25 mm/s, spot diameter: 0.6 mm	The equiaxed crystals of the parent material contain multiple phases, the weld zone is columnar dendrites, and the Al-Ni phase is dissolved. Welding weakens the Al-Ni segregation and reduces the β-bcc phase.
Kashaev *et al.* [66]	CoCrFeNiMn	Laser beam welding	Laser power: 2500W, focal position above the specimen surface: 0.0 mm, welding speed: 82 mm/s	The weld zone is an FCC matrix, with carbide precipitation and grain refinement occurring in the heat-affected zone.
Wu *et al.* [67]	CrMnFeCoNi	Electron beam welding	Power: 125000V, 5 mA, welding speed: 9.53 mm/s	The weld zone has an FCC structure, with deformation twins, and the grain size in the heat-affected zone grows.

CONFLICT OF INTEREST

The authors declare no conflict of interest.

AUTHOR CONTRIBUTIONS

ML conducted the research, draft preparation, data curation, formal analysis; MP writing, reviewing and editing, formal analysis; VC writing, formal analysis; SE reviewing and editing, formal analysis; all authors had approved the final version.

FUNDING

The Research on An Integrated Technology for Sustainable Development on Agricultural Industry by King Mongkut's Institute of Technology Ladkrabang (KMITL) has received funding support from the NSRF (FRB650028/0258).

REFERENCES

[1] C. O. Ujah, D. V. V. Kallon, and V. S. Aigbodion, "Study on properties of high entropy alloys reinforced with carbon nanotubes/graphene—A review," *Journal of Alloys and Metallurgical Systems*, vol. 8, 100117, 2024.

[2] I. J. Singh, Q. Murtaza, and P. Kumar, "A comprehensive review on effect of cold metal transfer welding parameters on dissimilar and similar metal welding," *Journal of Engineering Research*, vol. 13, pp. 1184–1201, 2025.

[3] R. E. Kubilay and W. A. Curtin, "Theory of twin strengthening in FCC high entropy alloys," *Acta Materialia*, vol. 216, 117119, 2025.

[4] A. Siddique, T. Abid, M. A. Akram *et al.,* "Design and development of NbTiVZr porous high entropy alloys for energy applications," *Journal of Energy Storage*, vol. 73, 109131, 2023.

[5] J. Xu, S. Peng, Z. Y. Li *et al.,* "Remarkable cavitation erosion-corrosion resistance of CoCrFeNiTiMo high-entropy alloy coatings," *Corrosion Science*, vol. 190, 109663, 2021.

[6] A. Jarlöv, Z. Zhu, W. Ji *et al.,* "Recent progress in high-entropy alloys for laser powder bed fusion: Design, processing, microstructure, and performance," *Materials Science and Engineering: R: Reports*, vol. 161, 10083, 2024.

[7] I. J. Singh, Q. Murtaza, and P. Kumar, "A comprehensive review on effect of cold metal transfer welding parameters on dissimilar and similar metal welding," *Journal of Engineering Research*, vol. 13, no. 2, pp. 1184–1201, 2025.

[8] A. Celott, L. Sandnes, Ø. Grong *et al.,* "Cold butt welding of dissimilar aluminum alloys: Characterization and interface bonding conditions," *Materials Science and Engineering: A*, vol. 897, 146279, 2024.

[9] Y. K. Yadav, M. A. Shaz, N. K. Mukhopadhyay *et al.,* "Formation of B2 phase and its stability in equiatomic Al-Cu-Fe-Ni-Ti high entropy alloy," *Journal of Alloys and Metallurgical Systems*, vol. 8, 100137, 2024.

[10] M. V. Kamal, S. Ragunath, M. H. S. Reddy *et al.,* "Recent advancements in lightweight high entropy alloys—A comprehensive review," *International Journal of Lightweight Materials and Manufacture*, vol. 7, no. 5, pp. 699–720, 2024.

[11] H. Hashimoto, S. Isobe, N. Hashimoto *et al.,* "Synthesis of Li-Mg-Al-Ti based lightweight high entropy alloys by mechanical alloying and investigation of conditions for solid solution formation," *Journal of Alloys and Metallurgical Systems*, vol. 4, 100037, 2023.

[12] M. Naseri, A. O. Moghadam, M. Anandkumar *et al.,* "Enhancing the mechanical properties of high-entropy alloys through severe plastic deformation: A review," *Journal of Alloys and Metallurgical Systems*, vol. 5, 100054, 2024.

[13] D. Wu, B. Li, Y. Shi *et al.,* "Effects of different Al contents on mechanical properties and high temperature oxidation resistance of $Al_xCoCr_{0.6}NiV_{0.6}$ high entropy alloy," *Journal of Alloys and Compounds*, vol. 1025, 180348, 2025.

[14] A. Akbari, R. Vafaei, H. Jamali *et al.,* "Effects of annealing and cold rolling on microstructural features, magnetic properties, tensile behavior and electrical resistance of $FeCoNi(MnAl)_x$ high entropy alloys," *Intermetallics*, vol. 175, 108521, 2024.

[15] P. K. Verma, A. Singh, and A. Kumar, "Microstructure evolution and magnetic characteristics of a novel high entropy alloy produced by mechanical alloying and spark plasma sintering," *Intermetallics*, vol. 175, 108488, 2024.

[16] X. Yang, H. Zhang, P. Dong *et al.,* "A study on the formation of multiple intermetallic compounds of friction stir processed high entropy alloy particles reinforced Al matrix composites," *Materials Characterization*, vol. 183, 111646, 2022.

[17] M. Ma, W. Wei, H. Zhang *et al.,* "Dissimilar gas tungsten arc welding of $AlCoCrFeNi_{2.1}$ eutectic high entropy alloy to 316L stainless steel," *Journal of Materials Research and Technology*, vol. 35, pp. 7065–7073, 2025.

[18] A. Kumar, A. Dhar, G. Thirunavukarasu *et al.,* "Effect of processing temperature on interface microstructure of diffusion welded joint of super-duplex stainless steel and zirconium alloy with nickel alloy interlayer," *Materials Chemistry and Physics*, vol. 322, 129312, 2024.

[19] J. Shen, R. E. Kim, J. He *et al.,* "Excellent strength/ductility synergy by optimization of post-weld heat treatment for gas metal arc welded CoCrFeMnNi high entropy alloys with 410 stainless filler wire: High-throughput thermodynamic modelling with experimental validation," *Materials & Design*, vol. 249, 113556, 2025.

[20] J. Cheng, G. Wang, W. Wang *et al.,* "Brazing of high entropy ceramic to Nb using a CoFeCrNiCu high-entropy alloy filler: Interfacial microstructure and mechanism," *Journal of Materials Research and Technology*, vol. 36, pp. 9198–9207, 2025.

[21] S. Meng, M. Zhang, Y. Han *et al.,* "Effect of bonding time on the interfacial microstructure and mechanical properties of diffusion bonded tungsten alloy/steel joints using CrFeCoNiCu high entropy alloy interlayer," *Journal of Materials Research and Technology*, vol. 33, pp. 9386–9393, 2024.

[22] D. Song, R. Wang, T. Wang *et al.,* "Interface strengthening mechanism of TZM/Q235 joint by ultrasonic-assisted electron beam welding with high entropy alloy interlayer," *International Journal of Refractory Metals and Hard Materials*, vol. 123, 106772, 2024.

[23] S. Manoochehri and M. S. Khorrami, "Friction stir welding of AA5010 aluminum alloy to St-12 carbon steel using cocrcufeni high entropy alloy interlayer," *Journal of Manufacturing Processes*, vol. 99, pp. 298–309, 2023.

[24] Y. Wang, P. Li, C. Zhao *et al.,* "A novel high entropy composite interlayer for diffusion bonding of TC4 titanium alloy to 316L stainless steel," *Materials Today Communications*, vol. 41, 110291, 2024.

[25] N. Jiang, H. Bian, X. Song *et al.,* "Contact-reactive brazing of CoCrFeMnNi high-entropy alloy to Zr alloys using Cu interlayer," *Materials Characterization*, vol. 204, 113186, 2023.

[26] X. Song, N. Jiang, H. Bian *et al.,* "Microstructure evolution and strengthening mechanism of CoCrFeMnNi HEA/Zr-3 brazed joints reinforced by fine-grained BCC HEA and HCP Zr," *Journal of Materials Science & Technology*, vol. 185, pp. 32–47, 2024.

[27] Z. Guo, Z. Li, W. Guo *et al.,* "Microstructural characteristics and mechanical response of transient liquid-phase diffusion bonding $AlCoCrFeNi_{2.1}$ high entropy alloy utilizing BNi-5 interlayer," *Journal of Alloys and Compounds*, vol. 1009, 176904, 2024.

[28] R. R. Kumar, R. K. Gupta, A. K. Shukla *et al.,* "Development of large-size dissimilar stainless steel/α-Ti alloy joints by diffusion bonding using vacuum hot press: Interface microstructure and tensile response in the temperature range of 77–773 K," *Materials Science and Engineering: A*, vol. 910, 146897, 2024.

[29] Y. Palguna, K. Sairam, A. R. Kannan *et al.,* "Effect of post weld heat treatment on the microstructure and mechanical properties of gas tungsten arc welded $Al_{0.3}CoCrFeNi$ high entropy alloy," *Scripta Materialia*, vol. 241, 115887, 2024.

[30] Y. Palguna, A. R. Kannan, K. Sairam *et al.,* "Microstructure and mechanical properties of wrought $Al_{0.2}CoCrFeNiMo_{0.5}$ high entropy alloy using gas tungsten arc welding process," *Materials Letters*, vol. 317, 132109, 2022.

[31] H. Esmaeilpoor, M. Aghaahmadi, H. J. Yoo *et al.,* "Mechanical response and microstructural evolution of a composite joint fabricated by green laser dissimilar welding of VCoNi medium entropy alloy and 17-4PH stainless steel," *Journal of Materials Science & Technology*, vol. 213, pp. 223–240, 2025.

[32] J. Liu, S. Wang, J. Wang *et al.,* "Laser beam weldability of TiZrHfNbTa high entropy alloy and dissimilar weldability to C103 refractory alloy," *International Journal of Refractory Metals and Hard Materials*, vol. 114, 106270, 2023.

[33] H. Yao, K. Chen, K. Kondoh *et al.,* "Microstructure and mechanical properties of friction stir lap welds between FeCoCrNiMn high entropy alloy and 6061 Al alloy," *Materials & Design*, vol. 224, 111411, 2022.

[34] H. Zhang, J. Miao, K. Wang *et al.,* "Interfacial reaction characteristics and mechanisms during dissimilar friction stir lap welding of pure copper and $Al_{0.1}CoCrFeNi$ alloy," *Journal of Materials Research and Technology*, vol. 31, pp. 1665–1674, 2024.

[35] J. Yang, D. Feng, Y. Liu *et al.,* "Excellent corrosion resistance of electron beam welded joint and remelted layer of eutectic high-entropy alloy $AlCoCrFeNi_{2.1}$," *Intermetallics*, vol. 154, 107822, 2023.

[36] Y. P. Lu, H. Jiang, S. Guo *et al.,* "A new strategy to design eutectic high-entropy alloys using mixing enthalpy," *Intermetallics*, vol. 91, pp. 124–128, 2017.

[37] R. J. Vikram, B. S. Murty, D. Fabijanic *et al.,* "Insights into micro-mechanical response and texture of the additively manufactured eutectic high entropy alloy $AlCoCrFeNi_{2.1}$," *Journal of Alloys and Compounds*, vol. 827, 154034, 2020.

[38] J. W. Yang, T. Li, Z. Li *et al.,* "Effect of welding speed on the thermal cycle and microstructure during laser welding of 2205 stainless steel," *Applied Laser*, vol. 44, no. 2, pp. 52–58, 2024.

[39] R. Sokkalingam, P. Mastanaiah, V. Muthupandi *et al.,* "Electron-beam welding of high-entropy alloy and stainless steel: microstructure and mechanical properties," *Materials and Manufacturing Processes*, vol. 35, no. 16, pp. 1885–1894, 2020.

[40] N. K. Adomako, G. Shin, N. Park *et al.,* "Laser dissimilar welding of CoCrFeMnNi-high entropy alloy and duplex stainless steel," *Journal of Materials Science & Technology*, vol. 85, pp. 95–105, 2021.
[41] Y. L. Liu, Y. C. Luo, and Y. Y. Shi, "Vacuum diffusion welding between CoCrFeMnNi high entropy and stainless steel," *Electric Welding Machine*, vol. 46, no. 12, pp. 122–127, 2016.
[42] P. Li, H. T. Sun, C. Li *et al.,* "A novel strengthening strategy for diffusion bonded joint of $AlCoCrFeNi_{2.1}$ eutectic high entropy alloy to 304 stainless steel," *Transactions of Nonferrous Metals Society of China*, vol. 33, no. 7, pp. 2121–2135, 2023.
[43] X. T. Zhang, J. Wang, Q. Xu *et al.,* "Microstructure evolution and shear strength in CoCrFeNi/AISI 304 joint by vacuum brazing with BNi-2 filler metal," *Journal of Materials Research and Technology*, vol. 33, pp. 8425–8434, 2024.
[44] J. Li, H. L. Zhao, N. Zhou *et al.,* "Diffusion bonding of CoCrFeNiCu high-entropy alloy to 304 Stainless steel," *Acta Metallurgica Sinica*, vol. 57, . 12, pp. 1567–1578, 2021.
[45] G. Wang, G. M. Sheng, Q. L. Yu *et al.,* "Investigation on regulating inter-granular penetration in CoCrMnFeNi high-entropy alloy and 304 stainless steel dissimilar joints," *Materials Science and Engineering: A*, vol. 800, 140291, 2021.
[46] A. Soleimani, M. Akbari, A. Karimipour *et al.,* "Investigation the effect of dissimilar laser welding parameters on temperature field, mechanical properties and fusion zone microstructure of inconel 600 and duplex 2205 stainless steel via response surface methodology," *Heliyon*, vol. 10, no. 4, e26010, 2024.
[47] A. Zarei, M. Akbari, A. Abdollahi *et al.,* "Experimental and numerical study of dissimilar fiber laser welding of martensitic AISI 1060 carbon steel with different configuration with austenitic 304 and ferritic 420 stainless steel," *Heliyon*, vol. 10, no. 21, e39954, 2024.
[48] P. K. Tao, X. Zhang, G. Y. Mi *et al.,* "Research on fiber laser welding formation, microstructure, and mechanical properties of 7.5 mm 304 stainless steel," *Journal of Materials Research and Technology*, vol. 24, pp. 236–249, 2023.
[49] Y. J. Du, J. T. Xiong, F. Jin *et al.,* "Microstructure evolution and mechanical properties of diffusion bonding $Al_5(TiZrHfNb)_{95}$ refractory high entropy alloy to Ti_2AlNb alloy," *Materials Science and Engineering: A*, vol. 802, 140610, 2021.
[50] Y. Peng, J. L. Li, J. M. Shi *et al.,* "Microstructure and mechanical properties of diffusion bonded joints of high-entropy alloy $Al_5(HfNbTiZr)_{95}$ and TC4 titanium alloy," *Journal of Materials Research and Technology*, vol. 11, pp. 1741–1752, 2021.
[51] Y. Lei, S. P. Hu, T. L. Yang *et al.,* "Vacuum diffusion bonding of high-entropy $Al_{0.85}CoCrFeNi$ alloy to TiAl intermetallic," *Journal of Materials Processing Technology*, vol. 278, 116455, 2020.
[52] P. Li, S. Wang, Y. Xia *et al.,* "Diffusion bonding of $AlCoCrFeNi_{2.1}$ eutectic high entropy alloy to TiAl alloy," *Journal of Materials Science& Technology*, vol. 45, pp. 59–69, 2020.
[53] A. Arab, Y. Guo, Q. Zhou *et al.,* "Joining AlCoCrFeNi high-entropy alloys and Al-6061 by explosive welding method," *Vacuum*, vol. 174, 109221, 2020.
[54] S. Y. Jiang, C. Cai, M. Zhao *et al.,* "Microstructure and properties of Q235 steel/6061 aluminum alloy resistance spot welded joints based on high entropy alloy interlayer," *Transactions of The China Welding Institution*, vol. 7, pp. 71–78, 2023.
[55] H. Azhari-Saray, M. Sarkari-Khorrami, A. Nademi-Babahadi *et al.,* "Dissimilar resistance spot welding of 6061-T6 aluminum alloy/St-12 carbon steel using a high entropy alloy interlayer," *Intermetallics*, vol. 124, 106876, 2020.
[56] X. Y. Gu and L. H. Zhang, "Laser lap welding of TC4 titanium alloy to 6082 aluminum alloy using a $CoNiCuNb_{0.5}V_{1.5}$ high entropy alloy filler," *Materials Letters*, vol. 312, 131562, 2022.
[57] J. Freudenberger, F. Thiel, D. Utt *et al.,* "Solid solution strengthening in medium- to high-entropy alloys," *Materials Science and Engineering: A*, vol. 861, 144271, 2022.
[58] N. A. Zarkevich, T. M. Smith, E. N. Baum *et al.,* "Compositional glass: A state with inherent chemical disorder, exemplified by Ti-rich $Ni_3(Al, Ti)$ $D0_{24}$ phase," *Crystals*, vol. 12, no. 8, 1049, 2022.
[59] Y. Lei, J. Sun, X. G. Song *et al.,* "Eutectic-reaction brazing of $Al_{0.3}CoCrFeNi$ high-entropy alloys using Ni/Nb/Ni interlayers," *Journal of Materials Science& Technology*, vol. 121, pp. 245–255, 2022.
[60] P. Li, H. T. Sun, S. Wang *et al.,* "Diffusion bonding of $AlCoCrFeNi_{2.1}$ eutectic high entropy alloy to GH4169 superalloy," *Materials Science and Engineering: A*, vol. 793, 139843, 2020.
[61] M. S. Zheng, S. W. Wu, X. Q. Si *et al.,* "Microstructure and mechanical properties of $Al_{0.3}CoCrFeNi$ high-entropy alloy joints brazed using a FeCoCrNiCu/Ti composite interlayer," *Journal of Materials Research and Technology*, vol. 30, pp. 6889–6896, 2024.
[62] X. P. Wu, W. Q. Zhang, H. M. Fu *et al.,* "Study on microstructure and properties of laser welded joint of dissimilar high entropy alloy CuCoCrFeNi and AlCoCrFeNi," *Materials Science and Technology*, vol. 25, no. 4, pp. 25–30, 2017.
[63] Z. G. Zhu, Y. F. Sun, F. L. Ng *et al.,* "Friction-stir welding of a ductile high entropy alloy: Microstructural evolution and weld strength," *Materials Science and Engineering: A*, vol. 711, pp. 524–532, 2018.
[64] H. Nam, S. Park, S. H. Shim *et al.,* "Enhancement of tensile properties applying phase separation with Cu addition in gas tungsten arc welds of CoCrFeMnNi high-entropy alloys," *Scripta Materialia*, vol. 220, 114897, 2022.
[65] R. Sokkalingam, K. Sivaprasad, and M. Duraiselvam, "Novel welding of $Al_{0.5}CoCrFeNi$ high-entropy alloy: Corrosion behavior," *Journal of Alloys and Compounds*, vol. 817, 153163, 2020.
[66] N. Kashaev, V. Ventzke, N. Petrov *et al.,* "Fatigue behaviour of a laser beam welded CoCrFeNiMn-type high entropy alloy," *Materials Science and Engineering: A*, vol. 76, 138358, 2019.
[67] Z. Wu, S. A. David, Z. Feng *et al.,* "Weldability of a high entropy CrMnFeCoNi alloy," *Scripta Materialia*, vol. 124, pp. 81–85, 2016.